LCCL-LC Resonant Converter and Its Soft Switching Realization for Omnidirectional Wireless Power Transfer Systems

Junjie Feng, *Member, IEEE*, Qiang Li, *Member, IEEE*, Fred C. Lee, *Life Fellow, IEEE*, and Minfan Fu, *Senior Member, IEEE*

***Abstract*—Recently, omnidirectional wireless power transfer (WPT) systems have been studied intensely, due to their improved flexibility as compared to their planar counterparts. The LCCL-LC resonant converter topology is selected due to its current source characteristics in this article. The system frequency is pushed to megahertz (MHz) to increase the spatial charging freedom. In a megahertz WPT system, the reactance of the full bridge rectifier can no longer be neglected; therefore, an analytical model of the full bridge rectifier input impedance is built. Furthermore, zero-voltage switching (ZVS) of the switching devices is essential in reducing the switching loss and noise in a megahertz system. A design methodology of the LCCL-LC circuit is proposed to achieve the ZVS operation in the case of one transmitter and one receiver. Then, the ZVS analysis is extended to the scenario of multiple transmitter coils and one receiver coil. Finally, a 6.78-MHz wireless charging system is built according to the proposed design methodology. Experimental results validate the accuracy of the ZVS analysis, and the ZVS operation is well achieved under different coupling and load conditions. The peak system efficiency of 82% at 5-W output power is achieved.**

***Index Terms*—Compensation network, wireless power transfer, resonant converter, zero-voltage switching (ZVS) switching.**

I. Introduction

WIRELESS power transfer (WPT) with loosely coupled coils is a promising solution to deliver power to a battery in a variety of applications. Due to its convenience, WPT technology has become popular in electric vehicles [1], [2], consumer electronics [3], [4], and medical devices [5], [6]. Thus far, the majority of the coupled coils in these systems are planar structure, and the magnetic field induced by the transmitter coil is in one direction, meaning that the energy power transfer capability degrades greatly when there is some angle misalignment between the coupled coils.

To improve the charging flexibility, a 3-D coils structure is utilized to transfer energy in different directions [7]–[12]. In [7], a bowl-shaped transmitter coils structure was reported to provide 3-D magnetic field distribution; however, it is pointed out in [8], that identical transmitter coil excitation current in [7] cannot generate true omnidirectional field distribution. Considering this, an omnidirectional WPT system with nonidentical excitation current control is proposed in [9]–[12]. In these systems, the magnetic field at any point is the vector sum of the magnetic field induced by each transmitter coil. The magnetic field induced by each transmitter coil is regarded as the basis vector. With a different ratio among different basis vectors, the total magnet field vector can be in different directions.

In an omnidirectional WPT system, the excitation current of each transmitter coil is controlled to induce the magnetic field in different directions [8], [12]. The cross-coupling among different transmitter coils and the receiver loading effect make the control of the excitation current much more complicated. Considering this, an *LC* compensation network with a load independent characteristic of transmitter coil current is added to simplify the system control [15]. To allow more design freedom, a capacitor in series with the transmitter coil is added, to adjust the system input impedance and achieve soft-switching for the semiconductor devices [16]. Meanwhile, a compensation capacitor in series with the receiver coil is the simplest topology to achieve the maximum power transfer efficiency [17]. Therefore, an LCCL-LC resonant converter in Fig. 1 is formed with the LCC/S compensation.

In consumer electronics applications, megahertz WPT systems are used to improve the charging spatial freedom [4]. The zero-voltage switching (ZVS) operation of the switching devices is essential in reducing the switching loss and the switching related electromagnetic interference (EMI) issue. In [19], the ZVS analysis in an LCCL-LC circuit is conducted without considering the rectifier reactance and the dead-time period. In a megahertz system, the rectifier reactance caused from junction capacitance of the diode can no longer be neglected [20], [21]. However, an analytical model of the full bridge rectifier reactance is lacked and the impact of the rectifier reactance on

Manuscript received February 14, 2020; revised May 29, 2020 and July 18, 2020; accepted September 9, 2020. Date of publication September 21, 2020; date of current version November 20, 2020. This work was supported by the Power Management Consortium in the Center for Power Electronics Systems, Virginia Tech. This paper was presented in part at 2019 IEEE Applied Power Electronics Conference and Exposition, Anaheim, CA, USA, March 17–21, 2019. Recommended for publication by Associate Editor C. K. Lee. *(Corresponding author: Qiang Li.)*

Junjie Feng, Qiang Li, and Fred C. Lee are with the Center for Power Electronics Systems, Virginia Tech, Blacksburg, VA 24061 USA (e-mail: junjie92@vt.edu; lqvt@vt.edu; fclee@vt.edu).

Minfan Fu was with the Center for Power Electronics Systems, Virginia Tech, Blacksburg, VA 24061 USA. He is now with the School of Information Science and Technology, Shanghai Tech University, Pudong 201210, China (e-mail: fumf@shanghaitech.edu.cn).

Color versions of one or more of the figures in this article are available online at https://ieeexplore.ieee.org.

Digital Object Identifier 10.1109/TPEL.2020.3024757

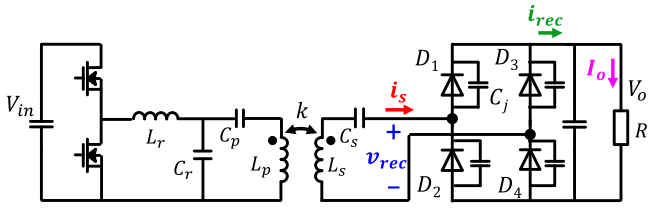

Fig. 1. LCCL-LC resonant converter.

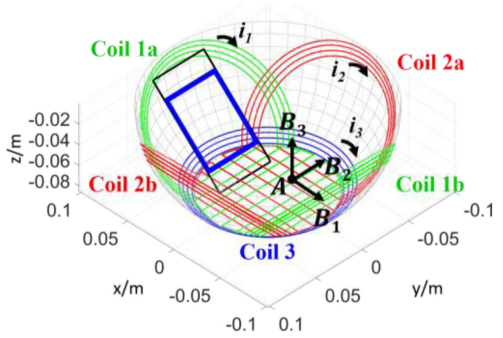

Fig. 2. Transmitter coils structure and a smart phone size receiver coil of the omnidirectional WPT system reported in [24].

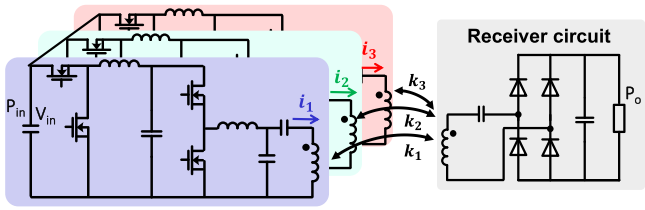

Fig. 3. System structure of the omnidirectional WPT system.

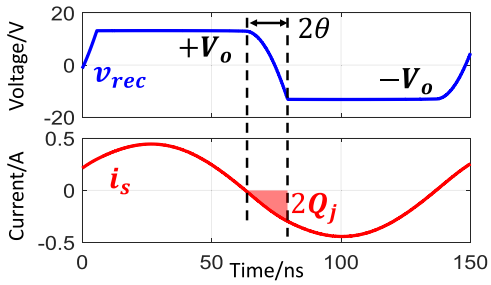

Fig. 4. Voltage and current waveform at the input port of the rectifier.

the ZVS operation of the LCCL-LC converter is not evaluated [20], [21]. Therefore, a comprehensive design methodology of a 6.78-MHz LCCL-LC resonant converter to achieve the ZVS operation, with considering the rectifier reactance and dead-time period, is proposed in Section II.

To improve the charging flexibility, a WPT system with multiple transmitter coils is normally adopted [22]–[24]. In these systems, the ZVS analysis is much more complicated; and it has never been conducted in the existing literature. Therefore, in this article, the ZVS analysis is extended to the case of multiple transmitter coils. Based on the analytical model, the ZVS condition is evaluated with different excitation current control methods in Section III. In Section IV, experimental results are given to verify the proposed design scheme. Finally, Section V concludes the article.

II. One Transmitter Case

A. Omnidirectional Charging Bowl System

The omnidirectional WPT system is gaining attention due to its charging flexibility as compared with its planar counterpart. In this article, the wireless charging bowl system reported in [24] is utilized as an example. The transmitter coils structure is shown in Fig. 2. There are three sets of coils: coils 1a and 1b, coils 2a and 2b, and coil 3. The magnetic field direction induced by each set of coils at point A is mainly in x, y, z directions, denoted as $\mathbf{B_1}$, $\mathbf{B_2}$, and $\mathbf{B_3}$. The total magnetic field at A is the vector sum of $\mathbf{B_1}$, $\mathbf{B_2}$, and $\mathbf{B_3}$, which is a function of the excitation current of each set of coils

$$\mathbf{B} = f(i_1)\mathbf{B_1} + f(i_2)\mathbf{B_2} + f(i_3)\mathbf{B_3}. \quad (1)$$

To simplify the system control, the load and coupling independent coil excitation current characteristic is desired. Regarding this, the LCC compensation network is adopted to drive these three sets of coils. The transmitter coil excitation current is determined by the input voltage and the impedance of the compensation inductor (L_r). To control the transmitter coil excitation current, a front buck stage is added for each channel, as shown in Fig. 3. By controlling the output voltage of the front buck, the amplitude of the excitation current (i_1, i_2, i_3) is controlled. Therefore, the magnetic field can be directed to any direction. In other words, there is omnidirectional magnetic field in such a system.

As shown in Fig. 2, when a smart phone device rests on the side face of the charging bowl, only coil 1 set should be excited to provide the energy; other transmitter coils are not excited. In this scenario, the system is simplified to one transmitter coil and one receiver. Meanwhile, the top device of the front buck is always ON to fully utilize the input voltage and maximize the power transfer capability. The circuit schematic for this case is shown in Fig. 1.

B. Rectifier Impedance

The LCCL-LC resonant converter, composed of a half bridge, resonant tank, and a full-bridge Schottky rectifier is shown in Fig. 1. At 6.78 MHz, the impact of the diode junction capacitance (C_j) can no longer be neglected [20], [21]. The voltage and current waveform at the input port of the full bridge rectifier is shown in Fig. 4. When the current flowing through D_1 and D_4 goes to zero, D_1 and D_4 are not turning OFF immediately. The negative current continues to flow through the junction capacitances of D_1 and D_4 and build a reverse voltage across the diodes. Therefore, the rectifier voltage v_{rec} lags the current i_s, due to the commutation of diodes, which leads to capacitive loading effect. Regarding this, an equivalent capacitance C_{eq} is

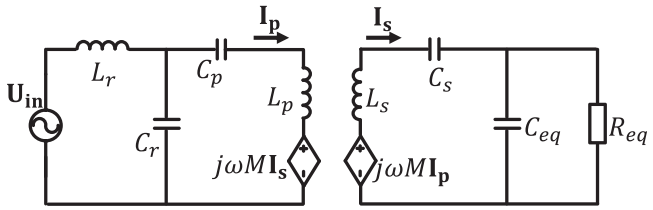

Fig. 5. Equivalent ac circuit of the LCCL-LC converter with fundamental approximation.

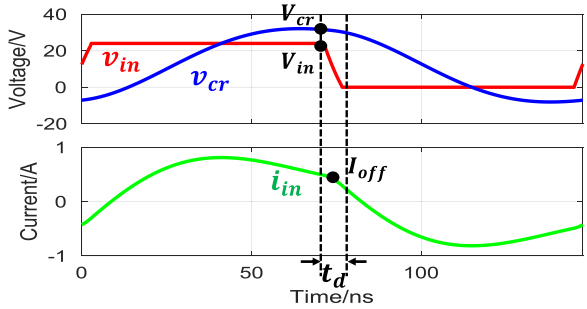

Fig. 6. Typical input voltage and current waveforms in the LCCL-LC circuit.

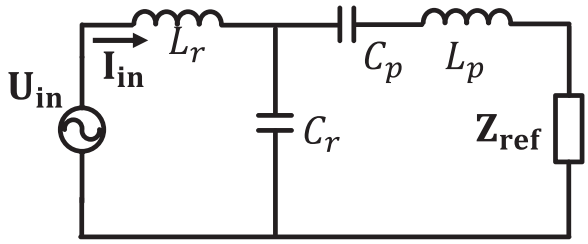

Fig. 7. Equivalent circuit of the LCCL-LC circuit with secondary side circuit reflected to primary side.

added in the ac equivalent circuit of the LCCL-LC converter with the fundamental approximation, as shown in Fig. 5. In Fig. 5, $\mathbf{U_{in}}$ is the fundamental component of the switching node voltage; R_{eq}, C_{eq} are utilized to model the rectifier impedance at the fundamental frequency. During the diode commutation period, the rectifier current (i_s) needs to remove the output junction charge ($2Q_j$) stored in diodes. According to the charge balance, the phase delay angle (θ) between the voltage and current of the rectifier can be solved. Then, the rectifier impedance can be derived. The expression of R_{eq} and C_{eq} is shown in (2). The full detailed derivation process is provided in the Appendix

$$C_{eq} = \frac{\pi^2 \sin\theta}{4\omega_o R(\cos(2\theta)+1)},\ R_{eq} = \frac{4R(\cos(2\theta)+1)}{\pi^2\cos\theta} \tag{2}$$

where $\theta = \sqrt{\frac{4RQ_j}{4RQ_j+V_oT}}$, Q_j is the junction charge stored at the diode junction cap.

C. Parameter Design for the ZVS Operation

The resonant frequency of the LCCL-LC converter is designed at the system frequency (6.78 MHz) as follows:

$$f_o = 1/2\pi\sqrt{L_rC_r} = 1/2\pi\sqrt{L_sC_s} = 6.78\ \text{MHz}. \tag{3}$$

At the resonant frequency of L_r and C_r, the equation of the transmitter coil current $\mathbf{I_p}$ in phasor diagram is shown in (4), which is independent of the coupling and load conditions [24]

$$\mathbf{I_p} = \frac{\mathbf{U_{in}}}{j\omega_o L_r}. \tag{4}$$

According to the Faraday's Law, the transmitter coil current induces a controlled voltage source in the receiver loop, as shown in Fig. 5. With the resonance of L_s and C_s, the voltage source directly applies to the input port of the rectifier. The amplitude of the fundamental component of the rectifier voltage at the resonant frequency (f_o) is derived as

$$V_{rec} = |j\omega_o M\mathbf{I_p}| = \left|j\omega_o M\frac{2/\pi V_{in}}{j\omega_o L_r}\right| = \frac{2k\sqrt{L_pL_s}}{\pi L_r}. \tag{5}$$

As shown in Fig. 4, the rectifier voltage waveform is trapezoidal in approximation, and the value of the upper plateau is the dc output voltage V_o. The phase angle of the diode commutation period is 2θ. According to the Fourier series expansion of a trapezoidal signal, the amplitude of the fundamental component of the rectifier voltage is

$$V_{rec} = \frac{4}{\pi}\frac{\sin(2\theta)}{2\theta}V_o \approx \frac{4}{\pi}V_o. \tag{6}$$

The diode commutation period is less than 15% of the whole switching period in a practical system ($\theta < 0.15\pi$); therefore, some approximation is made in (6). Combing (5) and (6), the output voltage of the converter is solved as

$$V_o = \frac{k\sqrt{L_pL_s}}{2L_r}V_{\text{in}}. \tag{7}$$

Here, k, L_p, and L_s are determined by the coil design; therefore, L_r is designed to satisfy the output voltage requirement. After L_r is determined, C_r can be determined according to (3). Meanwhile, the compensation capacitor C_s is designed to resonate with L_s at 6.78 MHz. Therefore, L_r, C_r, L_p, L_s, and C_s are determined, and there is only C_p left in the parameter design for the resonant tank in the LCCL-LC converter.

As for C_p, it is tuned to achieve ZVS with minimum circulating energy in the system. The typical input voltage, input current, and capacitor C_r voltage waveforms in the LCCL-LC resonant converter are shown in Fig. 6. To achieve ZVS, the turn-OFF current must be high enough to fully discharge the junction capacitor of the switching devices during a predetermined dead-time period (t_d). Herein, I_{off} is defined as the instant value of the input current at the middle point of the dead-time period ($t = T/2 = 1/2f_o$).

To calculate I_{off}, the equivalent circuit of the converter referred to the primary side is shown in Fig. 7, where $\mathbf{Z_{ref}}$ is the reflected frequency-dependent impedance of the receiver side circuit. In the equivalent circuit, v_{in} is a trapezoidal-wave voltage signal and is decomposed to different frequency components by Fourier series as

$$v_{in}(t) = \frac{V_{in}}{2} + \sum_{n=1,3,5\ldots}^{+\infty}\frac{\sin(n\pi f_o t_d)}{n\pi f_o t_d}\frac{2V_{in}}{n\pi}\sin(2n\pi f_o t). \tag{8}$$

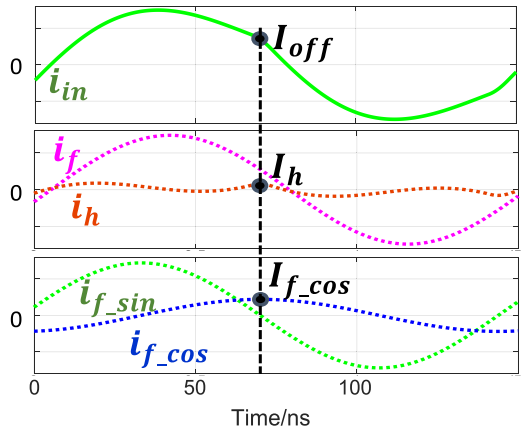

Fig. 8. Decomposition of the input current waveform in time domain.

If the input current component at each frequency is calculated correspondingly, I_{off} is the sum of the instant value of each component at $t = T/2$. To better visualize this process, the decomposition of the input current is shown in Fig. 8. The input current (i_{in}) is decomposed to its fundamental component (i_f) and harmonics component (i_h). Furthermore, the fundamental component is decomposed to two parts: sine ($i_{f\sin}$) and cosine ($i_{f\cos}$). The sine part is in phase with the input voltage and impacts the active power transfer of the system. On the contrary, the cosine part has a 90° phase difference with the input voltage and impacts the reactive power flowing in the system. As illustrated by Fig. 8, $i_{f\sin}$ equals zero at $t = T/2$ and does not contribute to I_{off}; however, $i_{f\cos}$ equals its amplitude at that time instant and contributes to I_{off} when the input impedance is inductive. Also, the harmonics component of the input current contributes to I_{off} and must be considered carefully.

With the equivalent circuit in Fig. 5, the KVL equation in the receiver loop is derived as

$$j\omega_o M\mathbf{I_p} + \mathbf{I_s}\left[j\omega_o L_s + \frac{1}{j\omega_o C_s} + \left(R_{eq}//\frac{1}{j\omega_o C_{eq}}\right)\right] = 0. \tag{9}$$

Then, the reflected impedance of the receiver circuit $\mathbf{Z_{ref}}$ at the fundamental frequency is calculated as

$$\mathbf{Z_{ref}} = \frac{j\omega_o M\mathbf{I_s}}{\mathbf{I_p}} = \frac{\omega_o^2 M^2}{R_{eq}}(1 + j\omega_o C_{eq} R_{eq}). \tag{10}$$

According to the equivalent circuit in Fig. 7, the complex input impedance at the fundamental frequency is derived as

$$\mathbf{Z_f} = \frac{L_r}{C_r}/\left[\mathbf{Z_{ref}} + j\left(\omega_o L_p - \frac{1}{\omega_o C_p} - \frac{1}{\omega_o C_r}\right)\right]. \tag{11}$$

The fundamental component of the input current in phasor domain ($\mathbf{I_f}$) is then calculated by the fundamental component input voltage ($\mathbf{V_f}$) divided by the input impedance

$$\mathbf{I_f} = \frac{\mathbf{V_f}}{\mathbf{Z_f}} = \frac{\mathbf{V_f}}{L_r/C_r}\frac{\omega_o^2 M^2}{R_{eq}} - j\frac{\mathbf{V_f}}{L_r/C_r}\left(\frac{1}{\omega_o C_p} + \frac{1}{\omega_o C_r} - \omega_o L_p - \omega_o^3 M^2 C_{eq}\right) \tag{12}$$

TABLE I
SPECIFICATIONS OF THE WPT SYSTEM

Specifications	Symbol	Practical Value
Input voltage	V_{in}	24V
Output voltage range	V_o	10~20V
Output power	P_o	5W
Switching frequency	f_o	6.78MHz
Transmitter coil self-inductance	L_p	3.09uH
Transmitter coil resistance	R_p	0.6Ω
Receiver coil self-inductance	L_s	4.7uH
Receiver coil resistance	R_s	0.6Ω
Coupling coefficient range	k	0.12~0.24

where $\mathbf{V}_f = \frac{\sin(\pi f_o t_d)}{\pi f_o t_d}\frac{2V_{in}}{\pi}\angle 0°$. In (12), there are two terms: the first term represents $i_{f\sin}$, which is in phase with $\mathbf{V_f}$, and the second term represents $i_{f\cos}$. As previously mentioned, only $i_{f\cos}$ contributes I_{off}, and its amplitude is derived as

$$I_{f\_\cos} = \frac{\sin(\pi f_o t_d)}{\pi f_o t_d}\frac{2V_{in}}{\pi}\frac{1}{\omega_o L_r} \times \left(1 - \frac{\omega_o L_p - 1/\omega_o C_p + \omega_o^3 M^2 C_{eq}}{\omega_o L_r}\right). \tag{13}$$

The high-order harmonics of input current in the LCCL-LC converter are actually trapped in L_r, C_r loop, due to the low-pass filter characteristics of the LC filter comprising of L_r and C_r. Similar to the fundamental component, the high-order harmonics in phasor domain ($\mathbf{I_h}$) are calculated as

$$\mathbf{I_h} = \sum_{n=3,5\ldots}^{+\infty}\frac{\mathbf{V_{h\_n}}}{\mathbf{Z_h}} = \sum_{n=3,5\ldots}^{+\infty}\frac{\mathbf{V_{h\_n}}}{jn\omega_o L_r + 1/jn\omega_o C_r} \tag{14}$$

where $\mathbf{V_{h\_n}} = \frac{\sin(n\pi f_o t_d)}{n\pi f_o t_d}\frac{2V_{in}}{n\pi}\angle 0°$.

At $t = T/2$, the harmonics components are at its peak value due to the 90° phase delay with the input voltage, and the instant value (I_h) is derived as

$$I_h = \sum_{n=3,5,7\ldots}^{+\infty}\frac{\sin(n\pi f_o t_d)}{n\pi f_o t_d}\frac{2V_{in}}{n\pi}\frac{1}{\omega_o L_r(n-1/n)}. \tag{15}$$

Then, the total turn-OFF current I_{off} is the sum of $I_{f\cos}$ and I_h

$$I_{off} = I_{f\_\cos} + I_h \approx \frac{\sin(\pi f_o t_d)}{\pi f_o t_d}\frac{2V_{in}}{\pi}\frac{1}{\omega_o L_r} \times \left(1.2 - \frac{\omega_o L_p - 1/\omega_o C_p + \omega_o^3 M^2 C_{eq}}{\omega_o L_r}\right). \tag{16}$$

In (16), the turn-OFF current is not only related to the value of C_p, but also the equivalent capacitance (C_{eq}) caused by the rectifier bridge. As illustrated by (2), C_{eq} is a function of the coupling and load condition, which makes the ZVS condition complicated. To demonstrate the quantitative impact of C_p and C_{eq} on the turn-OFF current, an example 6.78-MHz LCCL-LC converter for charging a smartphone device is designed. The specification of the example system is shown in Table I.

According to (7), the output voltage of the LCCL-LC circuit at f_o is proportional to k. A commercial Li-Ion battery charging chip, such as the TI BQ25703, can be cascaded after the resonant converter to charge the battery with a certain profile [25]. The

TABLE II
PASSIVE COMPONENTS VALUE IN THE LCCL-LC CIRCUIT

Component	L_r	C_r	C_s
Practical value	549nH	980pF	118pF

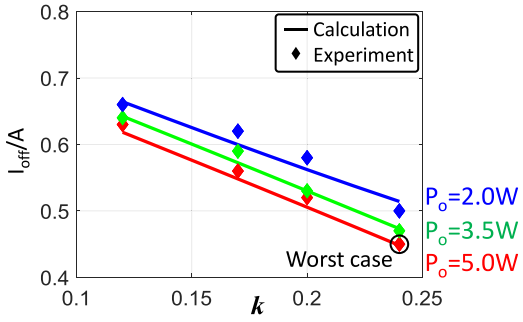

Fig. 9. Turn-OFF current of the designed system under different coupling coefficient and output power conditions.

typical input voltage range of the charging chip is 4–24 V. To reduce the conduction loss of the rectifier, a higher output voltage and lower current are preferred; therefore, the output voltage of the LCCL-LC converter is designed as 10–20 V. The value of L_r is designed to output 10 V at the worst coupling case ($k = 0.12$):

$$L_r = k_{\min}\sqrt{L_p L_s}V_{in}/2V_{o\min} = 549\,\text{nH}. \tag{17}$$

With L_r determined, the values of C_r and C_s are calculated according to (3). In summary, the designed values for the passive components in the LCCL-LC converter are listed in Table II. In the receiver circuit, four discrete DFLS130 diodes are adopted for the rectification, due to their small conduction voltage drop. After the rectifier bridge, a simple resistor is manually adjusted to maintain the output power.

With the specifications in Tables I and II, the turn-OFF current in different coupling coefficient and output power conditions under $C_p = 160$ pF, is shown in Fig. 9. As shown in Fig. 9, I_{off} reduces when the coupling coefficient (k) increases. An increase of coupling coefficient leads to large reflected impedance, so the impact of C_{eq} increases and the turn-OFF current reduces, according to (16). On the other hand, C_{eq} decreases as the output power decreases, due to the increase of the load resistance, according to (2). Regarding this, the turn-OFF current increases as the output power decreases, according to (16). In summary, the worst case for the turn-OFF current is the strong coupling and heavy load case. Therefore, C_p should be designed to achieve enough turn-OFF current to achieve ZVS at the worst case.

D. Considering Effect of the Dead-Time Period

To realize ZVS, the turn-OFF current must be able to fully discharge the equivalent junction capacitor (C_{oss}) of the switching devices during the dead-time period (t_d)

$$Q = \int_{(T-t_d)/2}^{(T+t_d)/2} i_{off}(t)dt \geq 2C_{oss}V_{in}. \tag{18}$$

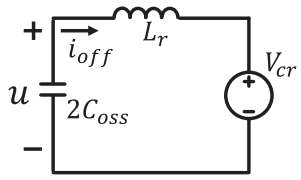

Fig. 10. Simplified equivalent circuit for the discharging of the junction cap of the switching devices during the dead-time period.

The turn-OFF current changes during t_d and the previously calculated I_{off} is the instant value at $t = T/2$. To calculate $i_{off}(t)$, the simplified equivalent circuit during t_d is derived in Fig. 10. Since the voltage of C_r does not change much during t_d, as shown in Fig. 6, C_r is replaced by a voltage source V_{cr}. The fundamental component of the voltage of C_r in phasor domain is calculated as

$$\mathbf{V_{cr}} = \frac{\mathbf{V_f}}{j\omega_o L_r}\left(j\omega_o L_p + \frac{1}{j\omega_o C_p} + \frac{\pi^2\omega_o^2 M^2}{8R}\right). \tag{19}$$

Then, the instant value of v_{cr} at $t = T/2$ is approximated by

$$V_{cr} \approx \left(\frac{1}{2} + \frac{\pi\omega_o M^2}{4RL_r}\right)V_{in}. \tag{20}$$

The second-order differential KVL equations in the equivalent circuit shown in Fig. 10, with the initial conditions, are derived as the following:

$$\begin{aligned} &2L_rC_{oss}\frac{d^2u(t)}{dt} - u(t) - V_{cr} = 0 \\ &2C_{oss}\frac{du(t)}{dt} = -i_{off}(t) \\ &u(0) = V_{in};\quad 2C_{oss}\frac{du(t_d/2)}{dt} = -I_{off}. \end{aligned} \tag{21}$$

Therefore, $i_{off}(t)$ is solved, and the discharge during t_d is calculated as

$$i_{off}(t) = I_1\sin(\omega_1 t + \varphi) \tag{22}$$

$$Q = 2C_{oss}(V_{in} - V_{cr}) - \frac{I_1}{\omega_1}\cos(\omega_1 t_d + \varphi) \tag{23}$$

where $I_1 = \frac{[I_{off} - \sin(\omega_1 t_d/2)(V_{in}-V_{cr})\omega_1 C_{oss}]^2}{\cos^2(\omega_1 t_d/2)} + (V_{in} - V_{cr})^2\omega_1^2 C_{oss}^2$

$$\varphi = arc\cos\frac{V_{in} - V_{cr}}{I_1}\omega_1 C_{oss};\ \omega_1 = \frac{1}{\sqrt{2L_rC_{oss}}}.$$

To realize the ZVS with minimum circulating energy, C_p is tuned so that the discharge (Q) during t_d is the same as the charge stored in the output junction capacitor (C_{oss}) of the primary devices for the worst case. Due to the complicacy of the model, an iterative program to solve C_p is built in MATLAB. The accuracy of the model is verified by experimental results in Section V.

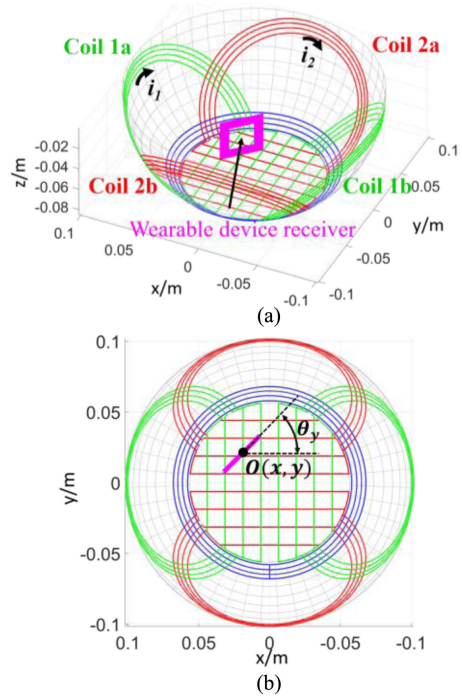

Fig. 11. Transmitter coils and a receiver coil in an omnidirectional WPT system [24]. (a) 3-D View. (b). Top view.

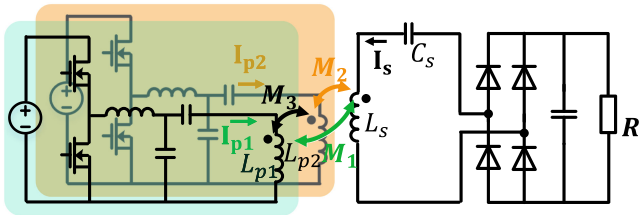

Fig. 12. Two-phase LCCL-LC circuit diagram with two transmitter coils.

III. Two Transmitter Case

A. I_{off} Calculation

In a multiple transmitter coils system, the ZVS condition is more complicated, due to the uncertain circulating energy incurred by different coils. To simplify the analysis, the ZVS condition with two transmitter coils is evaluated in this article. As shown in Fig. 11, when a wearable device receiver stands on the base of the charging bowl, coils 1a and 2a should be excited to provide the energy. It is worth noting that the orientation and position of the receiver coil in Fig. 11 are just an example and different transmitter coils should be excited according to positioning of the receiver coil.

The LCCL-LC circuit diagram with two transmitter coils is shown in Fig. 12. Herein, L_{p1}, L_{p2}, and L_s are the self-inductances of the two transmitter coils and receiver coil, respectively. M_1 and M_2 are the mutual inductance between the receiver coil and two transmitter coils; M_3 is the mutual inductance between the two transmitter coils. The decoupled circuit model

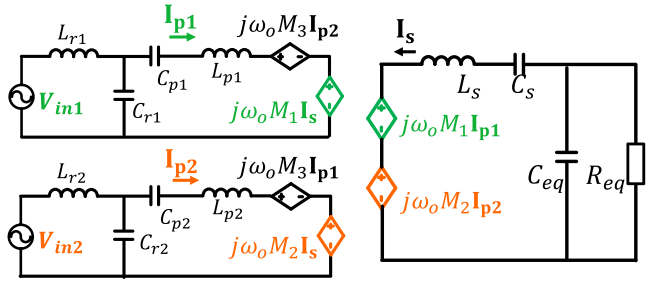

Fig. 13. Equivalent decoupled circuit at fundamental frequency.

at the fundamental frequency is shown in Fig. 13. The input voltage of each channel (V_{in1}, V_{in2}) is controlled by the front buck stages to implement the transmitter coil excitation current amplitude modulation. The KVL equation of the receiver circuit in phasor domain is derived as

$$j\omega_o M_1 \mathbf{I_{p1}} + j\omega_o M_2 \mathbf{I_{p2}} + \left(j\omega_o L_s + \frac{1}{j\omega_o C_s} + R_{eq} // \frac{1}{j\omega_o C_{eq}} \right) \mathbf{I_s} = 0. \quad (24)$$

At the resonant frequency of L_s and C_s, the receiver coil current is solved as follows:

$$\mathbf{I_s} = -(j\omega_o M_1 \mathbf{I_{p1}} + j\omega_o M_2 \mathbf{I_{p2}})(1 + j\omega_o R_{eq} C_{eq})/R_{eq}. \quad (25)$$

The complex reflected impedance in each transmitter circuit is derived as follows:

$$\mathbf{Z_{ref1}} = (j\omega_o M_1 \mathbf{I_s} + j\omega_o M_3 \mathbf{I_{p2}})/\mathbf{I_{p1}} \quad (26)$$

$$\mathbf{Z_{ref2}} = (j\omega_o M_2 \mathbf{I_s} + j\omega_o M_3 \mathbf{I_{p1}})/\mathbf{I_{p2}}. \quad (27)$$

Substituting (25) in (26) and (27), the reflected impedance in each transmitter circuit is solved as follows:

$$\mathbf{Z_{ref1}} = \left(\frac{\omega_o^2 M_1^2}{R_{eq}} + \frac{\omega_o^2 M_1 M_2}{R_{eq}} \frac{\mathbf{I_{p2}}}{\mathbf{I_{p1}}} \right) \times (1 + j\omega_o R_{eq} C_{eq}) + j\omega_o M_3 \frac{\mathbf{I_{p2}}}{\mathbf{I_{p1}}} \quad (28)$$

$$\mathbf{Z_{ref2}} = \left(\frac{\omega_o^2 M_2^2}{R_{eq}} + \frac{\omega_o^2 M_1 M_2}{R_{eq}} \frac{\mathbf{I_{p1}}}{\mathbf{I_{p2}}} \right) \times (1 + j\omega_o R_{eq} C_{eq}) + j\omega_o M_3 \frac{\mathbf{I_{p1}}}{\mathbf{I_{p2}}}. \quad (29)$$

After obtaining the reflected impedance for each transmitter circuit, the transmitter circuits are decoupled from one another. Then, the process to calculate the turn-OFF current for the one transmitter and one receiver case can be applied for the two transmitter case. The final turn-OFF current equations for each transmitter circuit are derived as follows:

$$I_{off1} \approx \frac{\sin(\pi f_o t_d)}{\pi f_o t_d} \frac{2V_{in1}}{\pi} \frac{1}{\omega_o L_{r1}} \times \left(1.2 - \frac{\omega_o L_{p1} - 1/\omega_o C_{p1} + \mathrm{Im}(\mathbf{Z_{ref1}})}{\omega_o L_{r1}} \right)$$

$$I_{off2} \approx \frac{\sin(\pi f_o t_d)}{\pi f_o t_d} \frac{2V_{in2}}{\pi} \frac{1}{\omega_o L_{r2}} \times \left(1.2 - \frac{\omega_o L_{p2} - 1/\omega_o C_{p2} + \mathrm{Im}(\mathbf{Z_{ref2}}))}{\omega_o L_{r2}}\right) \quad (30)$$

where $\mathrm{Im}(\mathbf{Z_{ref1,2}})$ is the imaginary part of the complex reflected impedance for two transmitter circuits

$$\mathrm{Im}(\mathbf{Z_{ref1}}) = C_{eq}\omega_o^3 M_1^2 + \mathrm{Im}\left[\left(\frac{\omega_o^2 M_1 M_2}{R_{eq}} + jC_{eq}\omega_o^3 M_1 M_2 + j\omega_o M_3\right)\frac{\mathbf{I_{p2}}}{\mathbf{I_{p1}}}\right]$$

$$\mathrm{Im}(\mathbf{Z_{ref2}}) = C_{eq}\omega_o^3 M_2^2 + \mathrm{Im}\left[\left(\frac{\omega_o^2 M_1 M_2}{R_{eq}} + jC_{eq}\omega_o^3 M_1 M_2 + j\omega_o M_3\right)\frac{\mathbf{I_{p1}}}{\mathbf{I_{p2}}}\right].$$

It is worth noting that the turn-OFF current equation becomes much more complicated compared to the one transmitter coil case. The excitation current of two transmitter coils has a significant impact on the turn-OFF current. In [8] and [9], the coil excitation current control methods are divided into two categories: there is phase difference among (i_1, i_2); there is no phase difference among (i_1, i_2)

$$Method\ I: \mathbf{I_{p1}} = I_m\angle 0^\circ,\ \mathbf{I_{p2}} = I_m\angle 90^\circ \quad (31)$$

$$\text{Method II}: \mathbf{I_{p1}} = m_1 I_m\angle 0^\circ,\ \mathbf{I_{p2}} = m_2 I_m\angle 0^\circ \quad (32)$$

where m_1 and m_2 are variables to control field direction.

Substituting (31) and (32) in (28) and (29), the imaginary part of the complex reflected impedance is derived as follows:$\mathbf{I_{p2}} = m_2 I_m\angle 0^\circ$

Method I:

$$\mathrm{Im}(\mathbf{Z}ref1) = C_{eq}\omega_o^3 M_1^2 + \frac{\omega_o^2 M_1 M_2}{R_{eq}} \quad (33)$$

$$\mathrm{Im}(\zeta\mathbf{r}ef2) = C_{eq}\omega_o^3 M_2^2 - \frac{\omega_o^2 M_1 M_2}{R_{eq}}. \quad (34)$$

Method II:

$$\mathrm{Im}(\mathbf{Z_{ref1}}) = C_{eq}\omega_o^3 M_1^2 + (C_{eq}\omega_o^3 M_1 M_2 + \omega_o M_3)\frac{m_2}{m_1} \quad (35)$$

$$\mathrm{Im}(\mathbf{Z_{ref2}}) = C_{eq}\omega_o^3 M_2^2 + (C_{eq}\omega_o^3 M_1 M_2 + \omega_o M_3)\frac{m_1}{m_2} \quad (36)$$

Therefore, the turn-OFF current for each channel is different for two current control methods. To achieve the ZVS operation in the operation range, the worst case for designing C_p is identified as follows.

B. Identify the Worst Case for Method I

The key advantage of an omnidirectional WPT system is that it can deal with angular misalignment of the receiver. The top view of a receiver device standing on the base of the bowl is shown in Fig. 11(b). Herein, the yaw rotation angle is defined as θ_y. The mutual inductance between the receiver coil and two transmitter coils, coil 1 set and coil 2 set, for different θ_y is shown in Fig. 14.

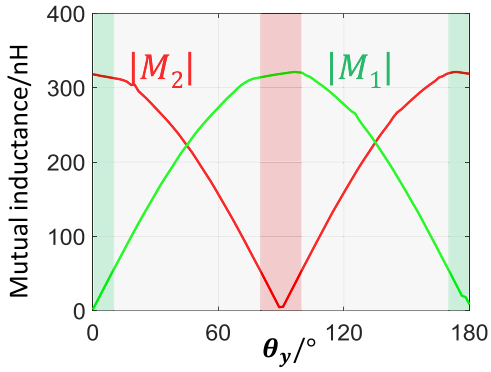

Fig. 14. Mutual inductance between receiver coil and transmitter coils 1a, coil 2a (M_1, M_2) versus different yaw angle θ_y of the receiver.

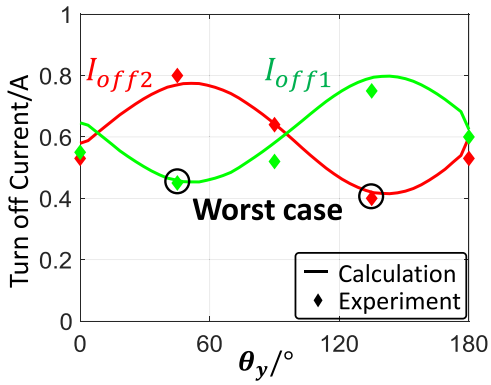

Fig. 15. Turn-OFF current of two transmitter circuits versus different yaw angle θ_y of the wearable receiver for modulation method I.

With the mutual inductance curve in Fig. 14, the turn-OFF current for the two transmitter coils circuit versus the different yaw rotating angles for modulation method I is shown in Fig. 15. There is large fluctuation in the turn-OFF current curve, and the turn-OFF current is smallest when $\mathrm{Im}(\mathrm{Z_{ref1,2}})$ is at the maximum value, based on (30). Similar to the one transmitter coil case, the worst case is the strong coupling and heavy load case, according to (33) and (34). The coupling condition refers to the product of M_1 and M_2 in the two transmitter coils case.

C. Identify the Worst Case for Method II

As for the current control method II, a buck stage is added before the LCCL-LC converter, to modulate the input voltage of the LCCL-LC converter and control the amplitude of the excitation current. According to [26], the best ratio between the amplitude of two transmitter coils current under the assumption that two coils' equivalent resistance is the same

$$m_1/m_2 = M_1/M_2. \quad (37)$$

Therefore, the input voltage of each channel in our system is controlled by the front buck as

$$V_{in1} = M_1/(M_1 + M_2)\cdot V_{in} = M_1/(M_1 + M_2)\cdot 24V \quad (38)$$

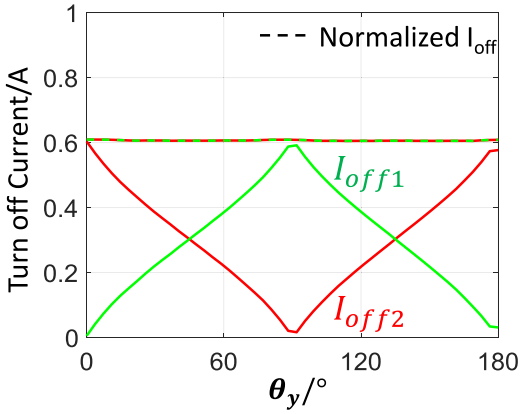

Fig. 16. Turn-OFF current of two transmitter circuits versus different yaw angle θ_y of the receiver for modulation method II when $M_3 = 0$.

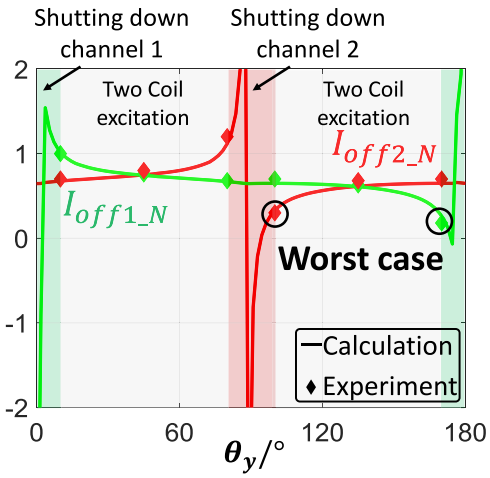

Fig. 17. Normalized turn-OFF current of two transmitter circuits versus different yaw angle θ_y of the receiver for modulation method II when $M_3 \neq 0$ ($k_3 = 0.05$).

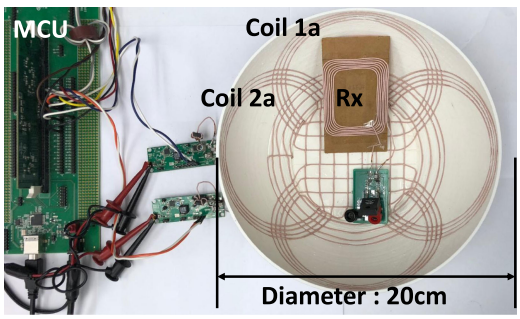

Fig. 18. Physical setup of the omnidirectional WPT system.

$$V_{in2} = M_2/(M_1 + M_2) \cdot V_{in} = M_2/(M_1 + M_2) \cdot 24\,V. \tag{39}$$

Substituting (37) in (35) and (36), the reflected impedance ($Z_{ref1,2}$) for method II is simplified as follows:

$$\mathrm{Im}(\mathbf{Z_{ref1}}) = C_{eq}\omega_o^3(M_1^2 + M_2^2) + \omega_o M_3 \frac{\boldsymbol{M_2}}{\boldsymbol{M_1}} \tag{40}$$

$$\mathrm{Im}(\mathbf{Z_{ref2}}) = C_{eq}\omega_o^3(M_1^2 + M_2^2) + \omega_o M_3 \frac{M_1}{M_2}. \tag{41}$$

As shown in (40) and (41), the mutual inductance between two transmitter coils (M_3) also impacts the reflected impedance and influences the turn-OFF current for each channel. In a multiple coils system, it is desired to reduce the circulating energy between different transmitter coils as much as possible. In other words, the mutual inductance between different transmitter coils should be minimized in the coil design stage. In this sense, the mutual inductance $M_3 = 0$ case is first studied. With the mutual inductance curve in Fig. 14, the turn-OFF current of the two channel circuit is shown in Fig. 16.

As shown in Fig. 16, turn-OFF current I_{off1} reduces as M_1 decreases. Meanwhile, the input voltage V_{in1} also reduces according to (38). With a smaller V_{in1}, the required turn-OFF current to achieve the ZVS operation also reduced proportionally. To better compare the turn-OFF current between the two modulation methods, the turn-OFF current for each channel in method II is normalized to full input voltage level. The normalization algorithm is as follows:

$$I_{off1\_N} = I_{off1} \cdot \frac{V_{in}}{V_{in1}}, \quad I_{off2\_N} = I_{off2} \cdot \frac{V_{in}}{V_{in2}}. \tag{42}$$

The normalized turn-OFF current curve versus θ_y for each channel in method II for $M_3 = 0$ case is shown as a dashed line in Fig. 16. Compared with method I, the turn-OFF current does not significantly change, which is beneficial for the ZVS operation. The physical reason behind this is the reflected impedance $Z_{ref1,\,2}$ in method II is determined by $M_1^2 + M_2^2$ according to (40) and (41). In a general omnidirectional WPT system, $M_1^2 + M_2^2$ does not significantly change as the angle misalignment changes. Therefore, the normalized turn-OFF current does not change much in method II. However, the reflected impedance $Z_{ref1,\,2}$ in method I is related to M_1M_2, which has large fluctuation for different angle misalignment.

The transmitter coils in an omnidirectional WPT system are normally symmetric structure, as reported in [9] and [10]. The mutual inductance between different transmitter coils in such a system is zero theoretically. However, there might be some weak cross-coupling due to the coil fabrication and terminations. Beside, in some multiple transmitter coils systems, such as systems reported in [12], [22], and [26], the cross-coupling between different transmitter coils also exists. Therefore, the impact of the cross-coupling on the turn-OFF current is evaluated as follows.

The normalized turn-OFF current curve for each channel is shown in Fig. 17 when the cross-coupling coefficient between two transmitter coils is 0.05. Here, there is a large glitch in the turn-OFF current curve for channel 2. The glitch exists at the red shaded zone, as plotted in Fig. 17. At the red zone, M_2 is small, and the cross-coupling term $\omega_o M_3 \frac{M_1}{M_2}$ will dominate the reflected impedance $Z_{ref2,}$ according to (41). This results in large fluctuation in the turn-OFF current curve. The ZVS operation can no longer be achieved when the turn-OFF current is negative. A similar phenomenon is also observed for the channel 1 case when M_1 is very small. In summary, the cross-coupling between

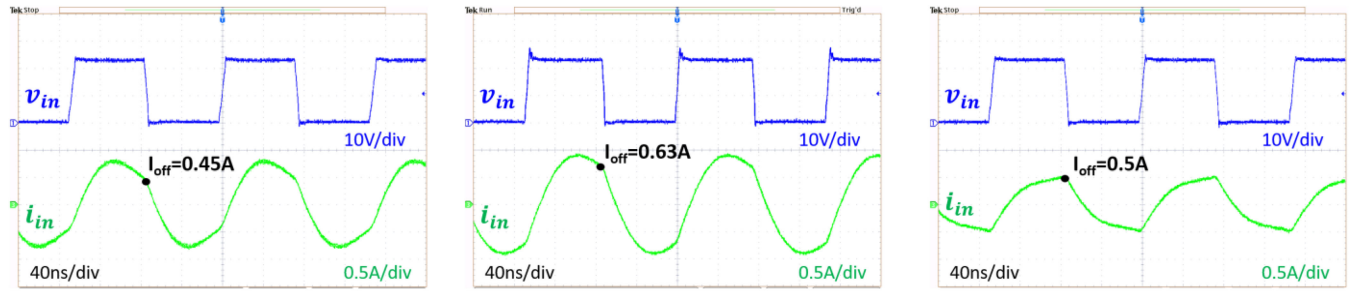

Fig. 19. Experimental switching node voltage and current waveform for one transmitter (coil 1a excited) and one receiver case (smart phone receiver Rx). (a) $k = 0.24$, $P_o = 5$ W (Worst case). (b) $k = 0.12$, $P_o = 5$ W. (c) $k = 0.24$, $P_o = 2$ W.

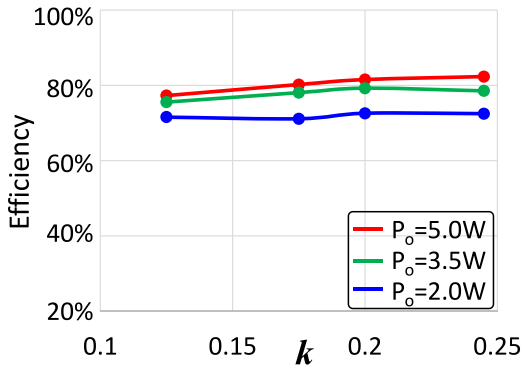

Fig. 20. Efficiency of the LCCL-LC converter in one transmitter case.

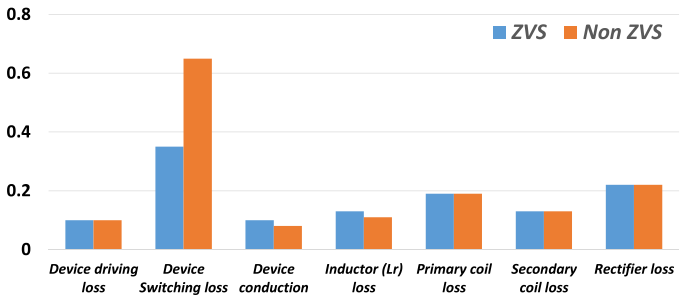

Fig. 21. Loss breakdown of the converter for ZVS and non-ZVS case. (Unit: W).

different transmitter coils deteriorates the ZVS condition when the ratio M_2/M_1 or M_1/M_2 is very large.

To solve this issue, channel 2 can be shut down in the glitch zone. The energy provided by channel 2 in the glitch zone is much smaller compared to channel 1, since M_2 is much smaller than M_1. Meanwhile, the operation efficiency also improves by shutting down one channel. As an example, the boundary condition to shut down channel 2 is $M_1/M_2 > 5$. Similarly, the boundary condition to shut down channel 1 is $M_2/M_1 > 5$. With this channel shading mechanism, the worst case for the turn-OFF current is at the boundary condition, as shown in Fig. 17. Therefore, C_{p1} should be designed to achieve enough turn-OFF current to achieve ZVS for channel 1 when $M_2/M_1 = 5$. Similarly, C_{p2} should be designed to achieve enough turn-OFF current to achieve ZVS for channel 2 when $M_1/M_2 = 5$.

IV. Experiment Verification

In this section, an omnidirectional wireless charging bowl is built, as shown in Fig. 18. In the experimental setup, there are two channel LCCL-LC circuits to drive the transmitter coils (coil 1a and coil 2a), separately. The TI microcontroller TMS320C28346 demo board is used to give the PWM signals to the half bridge of the LCCL-LC circuit, and the system is powered by an Agilent E3631A DC power source.

A. One Transmitter Case

As shown in Fig. 18, when a smart phone receiver device rests on the side face, coil 1a should be enabled to charge the receiver. The system is simplified to the case of one transmitter and one receiver, and the specifications for this case are shown in Tables I and II. In the transmitter side, the EPC8004 is adopted to operate at 6.78 MHz. The dead-time period is set as 5 ns. In the receiver circuit, four discrete DFLS130 diodes are adopted for the rectification due to their small conduction voltage drop. After the rectifier bridge, a simple resistor is manually adjusted to emulate the function of the battery charging chip.

To realize the ZVS operation at the worst case (strong coupling and heavy load), C_p is calculated as 160 pF, based on the analytical model in Section II. The turn-OFF current measurement results under different conditions are shown in Fig. 9. The measurement result matches very well with the analytical model. The switching node voltage and current waveform under three example conditions are shown in Fig. 19. The turn-OFF current is smallest at the strong coupling and heavy load case, which verifies the worst-case analysis. With the proposed designed methodology, the turn-OFF current is high enough for different conditions, and the ZVS operation is guaranteed, as illustrated by Fig. 19. The efficiency of the LCCL-LC circuit under different conditions is shown in Fig. 20. To verify the benefit of the ZVS operation, the loss breakdown of the converter when $k = 0.2$ and $P_o = 5$ W under the ZVS case and non-ZVS case is shown in Fig. 21. For the non-ZVS case, C_p increased to 180 pF to reduce the turn-OFF current to zero and minimize the circulation energy in the system. The switching loss at 6.78 MHz is greatly reduced with the ZVS operation and efficiency increases from 77.2% to 80.5%.

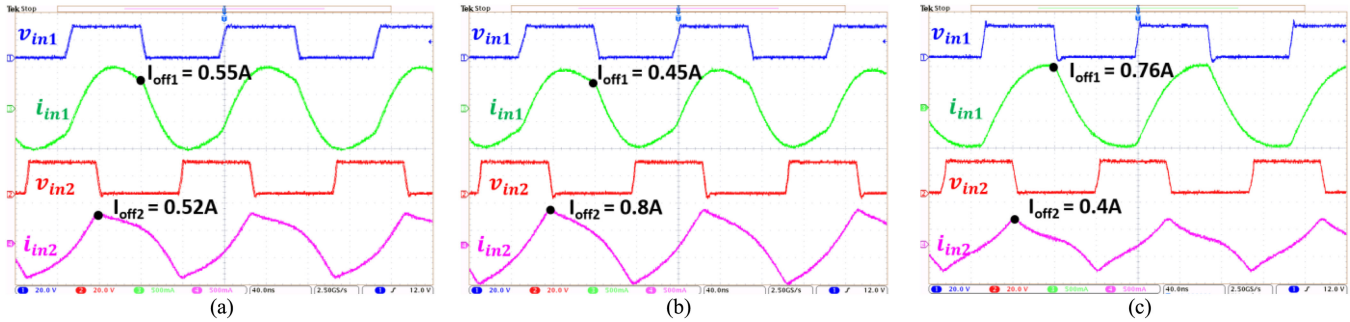

Fig. 22. Experimental switching node voltage and current waveform for two transmitter and one receiver case with excitation current method I. (a). $\theta_y = 0°$, $P_o = 2.5$ W. (b). $\theta_y = 45°$, $P_o = 2.5$ W (worst case for channel I). (c). $\theta_y = 135°$, $P_o = 2.5$ W (worst case for channel II).

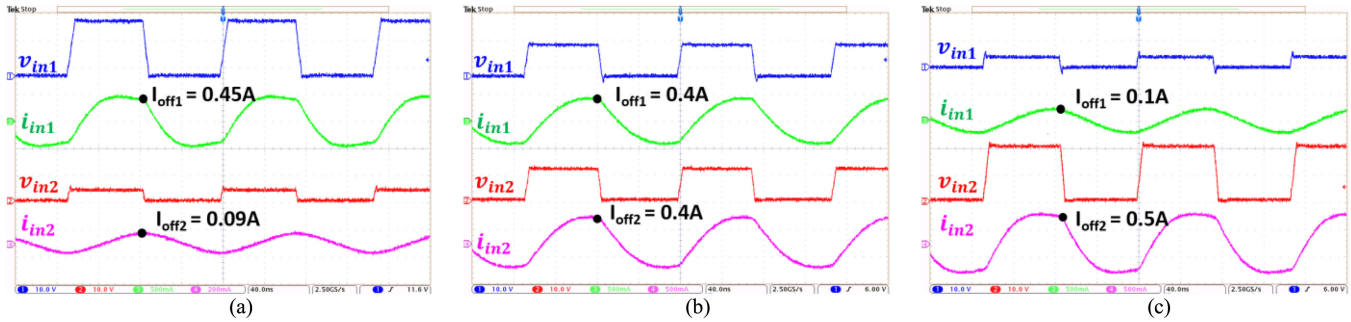

Fig. 23. Experimental switching node voltage and current waveform for two transmitter and one receiver case with excitation current method II. (a) $\theta_y = 100°$, $P_o = 2.5$ W ($M_1/M_2 = 5$, worst case for channel II). (b) $\theta_y = 135°$, $P_o = 2.5$ W. (c). $\theta_y = 170°$, $P_o = 2.5$ W ($M_2/M_1 = 5$, worst case for channel I).

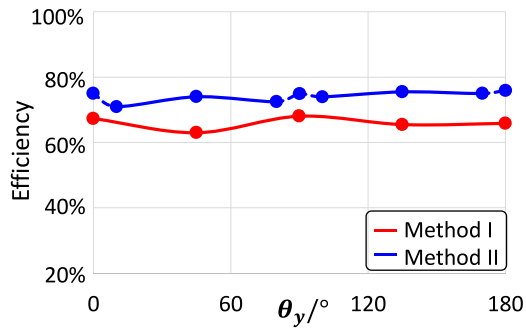

Fig. 24. System efficiency versus different yaw angle θ_y of the receiver for two transmitter and one receiver case.

B. Two Transmitter Case

As shown in Fig. 11, when a wearable device like smart watch device stands on the base of the charging bowl, coils 1a and 2a should be excited to provide the energy. In the test, a 35 × 35 mm^2 receiver coil (7.5 μH, 1.1 Ω), which is different from previous smart phone receiver coil, is fabricated to emulate an Apple watch receiver in the charging bowl. The two transmitter circuits to drive coil 1a and coil 2a are exactly the same, and the circuit specifications are shown in Tables I and II.

As mentioned by Section III, the turn-OFF current is related to the transmitter coil excitation current. As for current control method I, C_{p1} and C_{p2} are calculated as 155 pF to achieve the ZVS operation at the worst case based on (18) and (30). The turn-OFF current measurement results under different yaw angles of the receiver are shown in Fig. 15. The measurement results match with the calculation results very well. The experimental switching node voltage and current waveform for two channel LCCL-LC circuits, under three example receiver angles, are shown in Fig. 22. As demonstrated by Fig. 22, the turn-OFF current is high enough to achieve the ZVS operation for different orientations of the receiver devices.

As for excitation current method II, C_{p1} and C_{p2} are calculated as 162 pF to achieve the ZVS operation at the worst case based on (18) and (30). Then, the normalized turn-OFF current measurement results under different yaw angles of the receiver are shown in Fig. 17. The measurement results match with the calculation results very well. The experimental switching node voltage and current waveform for two channel LCCL-LC circuits, under three example receiver angles, are shown in Fig. 23. As demonstrated by Fig. 23, the turn-OFF current is high enough to achieve the ZVS operation for the different cases.

With the proposed design methodology, ZVS operation is well achieved under different conditions. The system efficiency at 2.5 W, (defined as the load power divided by the input power of the dc input source in Fig. 3), for two current control methods are shown in Fig. 24. The system efficiency in method II is better than method I. In method I, the input voltage of two channel LCCL-LC circuits is always 24 V and the rotating field is achieved by the phase difference between the two channels. However, the input voltage is adaptive according to the receiver's angle in method II. With lower input voltage, the switching loss and coil conduction loss in the transmitter side are smaller. Therefore, the system efficiency for method II is better.

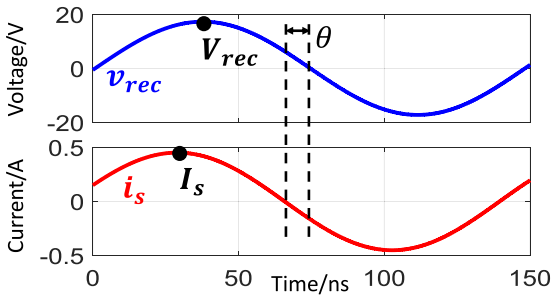

Fig. 25. Voltage and current waveform of the rectifier with fundamental approximation.

V. Conclusion

In this article, an analytical model of the full bridge rectifier input impedance including the effect of diode junction charge is built in a megahertz system. After considering the rectifier reactance, input impedance of the LCCL-LC circuit is dependent on the loading and coupling conditions. The strong coupling, heavy load case is identified as the worst case for the ZVS achievement. A passive component parameter design methodology is proposed to achieve the ZVS operation at the worst case. Then, the ZVS analysis is extended to a two transmitter coils case. The worst case for different excitation current control methods is identified in the two transmitter coils case, and the ZVS operation is guaranteed in different scenarios with the proposed design methodology. With the ZVS operation for primary switching devices, the total system efficiency of our system is in 62%–82%.

Appendix

The LCCL-LC circuit schematic, with consideration of the diode junction cap, is shown in Fig. 1. The voltage and current waveform of the rectifier bridge is shown in Fig. 4. Due to the commutation of diodes, the rectifier voltage, (v_{rec}) lags the current (i_s), which leads to the capacitive loading effect. During the diode commutation period, the rectifier current must remove the output junction charge ($2Q_j$) stored in the diodes. The charge balance equation is

$$\int_0^{2\theta/\omega_o} I_s \sin(\omega_o t)dt = 2Q_j \tag{43}$$

where I_s is the amplitude of the current flowing through the receiver loop.

To model the capacitive reactance in the receiver loop, an equivalent capacitance C_{eq} is added in the ac equivalent circuit, as shown in Fig. 5. With fundamental approximation, the voltage and current waveform of the rectifier bridge is shown in Fig. 25. The phase angle between the voltage and current waveform is θ. The real and imaginary parts of the admittance seen from the rectifier input port are calculated as

$$\frac{I_s}{V_{rec}}\cos\theta = \frac{1}{R_{eq}} \tag{44}$$

$$\frac{I_s}{V_{rec}}\sin\theta = \omega_o C_{eq} \tag{45}$$

where V_{rec} is the amplitude of the fundamental component of the rectifier voltage $V_{rec} \approx \frac{4}{\pi}\frac{\sin(2\theta)}{2\theta}V_o$.

According to (45), V_o and I_s are needed to solve the equivalent capacitance C_{eq}. In a steady state, the average current flowing through the output capacitor would be zero. Therefore, the average current flowing after the rectifier (i_{rec}) equals the load current (I_o) as defined in Fig. 1

$$\left[\int_0^{T/2} I_s \sin(\omega_o t)dt - 2Q_j\right] / \left(\frac{T}{2}\right) = I_o = \frac{V_o}{R}. \tag{46}$$

Combining (43)–(46), there is no simple analytical solution for C_{eq}. When the discharging period (2θ) is less than 15% of the whole charge period, some approximation is made

$$\frac{\sin(2\theta)}{2\theta} \approx 1. \tag{47}$$

With the approximation, the analytical solution of C_{eq} and R_{eq} is obtained as

$$C_{eq} = \frac{\pi^2 \sin\theta}{4\omega_o R(\cos(2\theta)+1)},\ R_{eq} = \frac{4R(\cos(2\theta)+1)}{\pi^2\cos\theta} \tag{48}$$

where $\theta = \sqrt{\frac{4RQ_j}{4RQ_j+V_oT}}$.

References

[1] C. C. Mi, G. Buja, S. Y. Choi, and C. T. Rim, "Modern advances in wireless power transfer systems for roadway powered electric vehicles," *IEEE Trans. Ind. Electron.*, vol. 63, no. 10, pp. 6533–6545, Oct. 2016.

[2] S. Kim, G. A. Covic, and J. T. Boys, "Tripolar pad for inductive power transfer systems for EV charging," *IEEE Trans. Power Electron.*, vol. 32, no. 7, pp. 5045–5057, Jul. 2017.

[3] S. Y. R. Hui, W. X. Zhong, and C. K. Lee, "A critical review on recent progress of mid-range wireless power transfer," *IEEE Trans. Power Electron.*, vol. 29, no. 9, pp. 4500–4511, Sep. 2014.

[4] M. Liu, C. Zhao, J. Song, and C. Ma, "Battery charging profile-based parameter design of a 6.78-MHz class E2 wireless charging system," *IEEE Trans. Ind. Electron.*, vol. 64, no. 8, pp. 6169–6178, Aug. 2017.

[5] O. Knecht, R. Bosshard, and J. W. Kolar, "High-efficiency transcutaneous energy transfer for implantable mechanical heart support systems," *IEEE Trans. Power Electron.*, vol. 30, no. 11, pp. 6221–6236, Nov. 2015.

[6] C. Xiao, D. Cheng, and K. Wei, "An LCC-C compensated wireless charging system for implantable cardiac pacemakers: Theory, experiment, and safety evaluation," *IEEE Trans. Power Electron.*, vol. 33, no. 6, pp. 4894–4905, Jun. 2018.

[7] E. R. Green, M. R. Bynum, and N. A. Redfield, "Wireless charging device having concave charging station," U.S. Patent 0188339, Jul. 2, 2015.

[8] W. Ng, C. Zhang, D. Lin, and S. Hui, "Two- and three dimensional omnidirectional wireless power transfer," *IEEE Trans. Power Electron.*, vol. 29, no. 9, pp. 4470–4474, Jan. 2014.

[9] C. Zhang, D. Lin, and S. Y. Hui, "Basic control principles of omnidirectional wireless power transfer," *IEEE Trans. Power Electron.*, vol. 31, no. 7, pp. 5215–5227, Jul. 2016.

[10] B. H. Choi, E. S. Lee, Y. H. Sohn, G. C. Jang, and C. T. Rim, "Six degrees of freedom mobile inductive power transfer by crossed dipole Tx and Rx coils," *IEEE Trans. Power Electron.*, vol. 31, no.4, pp. 3252–3272, Apr. 2016.

[11] N. Ha-Van and C. Seo, "Analytical and experimental investigations of omnidirectional wireless power transfer using a cubic transmitter," *IEEE Trans. Ind. Electron.*, vol. 65, no. 2, pp. 1358–1366, Feb. 2018.

[12] J. Feng, Q. Li, F. C. Lee, and M. Fu, "Transmitter coils design for free-positioning omnidirectional wireless power transfer system," *IEEE Trans. Ind. Inform.*, vol. 15, no. 8, pp. 4656–4664, Aug. 2019.

[13] W. Zhang and C. C. Mi, "Compensation topologies of high-power wireless power transfer systems," *IEEE Trans. Veh. Technol.*, vol. 65, no. 6, pp. 4768–4778, Jun. 2016.

[14] X. Qu, Y. Jing, H. Han, S. Wong, and C. K. Tse, "Higher order compensation for inductive-power-transfer converters with constant-voltage or constant-current output combating transformer parameter constraints," *IEEE Trans. Power Electron.*, vol. 32, no. 1, pp. 394–405, Jan. 2017.

[15] H. Hao, G. A. Covic and J. T. Boys, "An approximate dynamic model of LCL-T-based inductive power transfer power supplies," *IEEE Trans. Power Electron.*, vol. 29, no. 10, pp. 5554–5567, Oct. 2014.
[16] S. Li, W. Li, J. Deng, T. D. Nguyen, and C. C. Mi, "A double-sided LCC compensation network and its tuning method for wireless power transfer," *IEEE Trans. Veh. Technol.*, vol. 64, no. 6, pp. 2261–2273, Jun. 2015.
[17] W. X. Zhong and S. Y. R. Hui, "Maximum energy efficiency tracking for wireless power transfer systems," *IEEE Trans. Power Electron.*, vol. 30, no. 7, pp. 4025–4034, Jul. 2015.
[18] R. Tseng, B. von Novak, S. Shevde, and K. A. Grajski, "Introduction to the alliance for wireless power loosely-coupled wireless power transfer system specification version 1.0," *Proc. IEEE Wireless Power Transfer*, Perugia, Italy, 2013, pp. 79–83.
[19] Y. Wang, H. Wang, T. Liang, X. Zhang, D. Xu, and L. Cai, "Analysis and design of an LCC/S compensated resonant converter for inductively coupled power transfer," in *Proc. IEEE Transp. Electrif. Conf. Expo.*, Asia-Pacific, Harbin, China, 2017, pp. 1–5.
[20] M. Fu, Z. Tang, and C. Ma, "Analysis and optimized design of compensation capacitors for a megahertz WPT system using full-bridge rectifier," *IEEE Trans. Ind. Informat.*, vol. 15, no. 1, pp. 95–104, Jan. 2019.
[21] S. Park and J. M. Rivas, "Design of a class-DE rectifier with shunt inductance and nonlinear capacitance for high-voltage conversion," *IEEE Trans. Power Electron.*, vol. 33, no. 3, pp. 2282–2294, Mar. 2018.
[22] D. Ahn and S. Hong, "Effect of coupling between multiple transmitters or multiple receivers on wireless power transfer," *IEEE Trans. Ind. Electron.*, vol. 60, no. 7, pp. 2602–2613, Jul. 2013.
[23] Q. Zhu, M. Su, Y. Sun, W. Tang, and A. P. Hu, "Field orientation based on current amplitude and phase angle control for wireless power transfer," *IEEE Trans. Ind. Electron.*, vol. 65, no. 6, pp. 4758–4770, Jun. 2018.
[24] J. Feng, Q. Li, and F. C. Lee, "Coil and circuit design of omnidirectional wireless power transfer system for portable device application," in *Proc. IEEE Energy Convers. Congr. Expo.*, Portland, OR, USA, 2018, pp. 914–920.
[25] Texas Instruments. "I2C multi-chemistry battery buck-boost charge controller with system power monitor and processor hot monitor," bq25703A Datasheet, May 2017.
[26] C. Zhang, D. Lin, and S. Y. R. Hu, "Efficiency optimization method of inductive coupling wireless power transfer system with multiple transmitters and single receiver," in *Proc. IEEE Energy Convers. Congr. Expo.*, Milwaukee, WI, USA, 2016, pp. 1–6.

Junjie Feng (Student Member, IEEE) received the B.S. degree in electrical engineering from Xi'an Jiaotong University, Xi'an, China, in 2014. He is currently working toward the Ph.D. degree with the Center for Power Electronics Systems, Virginia Tech, Blacksburg, VA, USA.

His research interests include high-frequency power conversion, wireless power transfer, and resonant converters.

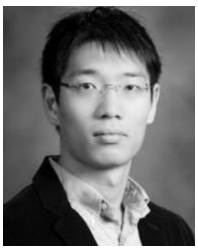

Qiang Li (Member, IEEE) received the B.S. and M.S. degrees in power electronics from Zhejiang University, Hangzhou, China, in 2003 and 2006, respectively, and the Ph.D. degree in electrical engineering from Virginia Tech, Blacksburg, VA, USA, in 2011.

He is currently an Associate Professor with the Center for Power Electronics Systems, Virginia Tech. His research interests include power management for distributed power systems, applications of wide-bandgap power devices, high-frequency power conversion and controls, magnetics and EMI, high-density electronics packaging and integration, and renewable energy.

Dr. Li received the First Place Prize Paper Award for 2016 in the IEEE TRANSACTIONS ON POWER ELECTRONICS. He is also a recipient of the 2017 National Science Foundation Career Award.

Fred C. Lee (Life Fellow, IEEE) received the B.S. degree from the National Cheng Kung University, Tainan City, Taiwan, in 1968, and the M.S. and Ph.D. degrees from Duke University, Durham, NC, USA, in 1972 and 1974, respectively, all in electrical engineering.

He is a University Distinguished Professor Emeritus with Virginia Polytechnic Institute and State University (Virginia Tech), Blacksburg, VA, USA, and the Founder and Director Emeritus of the Center for Power Electronics Systems, an Engineering Research Center consisting of 80 corporations. His research interests include high-frequency power conversion, magnetics and EMI, distributed power systems, renewable energy, power quality, high-density electronics packaging and integration, and modeling and control. He holds 94 U.S. patents, and has published more than 310 journal articles and more than 740 refereed technical papers. During his tenure at Virginia Tech, he has supervised to completion 87 Ph.D. and 93 master's students.

Dr. Lee was the President of the IEEE Power Electronics Society from 1992 to 1994 and a recipient of the William E. Newell Power Electronics Award in 1989; the PCIM Award for Leadership in Power Electronics Education presented at HFPC in 1990; the Arthur E. Fury Award for Leadership and Innovation in1998; the Honorary Sun Yuen Chuan Chair Professor of National Tsing Hua University in Taiwan in 2001; the Ernst-Blickle Award sponsored by SEW-EURODRIVE Foundation in 2005; the Distinguished Alumni Award from National Cheng Kung University in 2006; the Honorary Li Kwoh-Ting Chair Professor of National Cheng Kung University in 2011; and Inaugural Member of the Virginia Tech Entrepreneur Hall of Fame in 2012; an Honorary Chair Professor of National Chiao Tong University in Taiwan, in 2014; an Honorary Chair Professor of Tsinghua University in China, in 2017; and an Honorary Professor of the Huazhong University of Science and Technology in China, in 2018. He is a member of the U.S. National Academy Of Engineering, an Academician of the Academia Sinica in Taiwan, and a Foreign Member of the Chinese Academy of Engineering in the People's Republic of China. He is a recipient of the IEEE Medal in Power Engineering in 2015 "for contributions to power electronics, especially high-frequency power conversion," the Power Supply Technology Outstanding Achievement Award from China Power Supply Society in 2017, and was elected as a National Academy of Inventors Fellow in 2018.

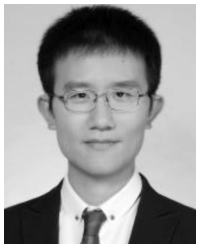

Minfan Fu (Member, IEEE) received the B.S., M.S., and Ph.D. degrees in electrical and computer engineering from the University of Michigan-Shanghai Jiao Tong University Joint Institute, Shanghai Jiao Tong University, Shanghai, China, in 2010, 2013, and 2016, respectively.

He is currently an Assistant Professor with the School of Information Science and Technology, ShanghaiTech University, Shanghai, China. From 2016 to 2018, he held a postdoctoral position with the Center for Power Electronics Systems, Virginia Polytechnic Institute and State University, Blacksburg, VA, USA. His research interests include megahertz wireless power transfer, high-frequency power conversion, high-frequency magnetic design, and application of wide-band-gap devices.